Detailed Low Temperature Studies on Thermoelectric Performance of K-doped $Bi_2Ca_2Co_2O_y$ Ceramics Fibers

C. Özçelik[1,3], T. Depci[1], G. Çetin[2], M. Gürsul[2], B. Özçelik[2*], M. A. Madre[3], A. Sotelo[3], H. Ando[4], K. Terashima[4], Y. Takano[4]
[1]Iskenderun Technical University, Institute of Engineering and Sciences, Hatay, Turkey
[2]Department of Physics, Faculty of Sciences and Letters, Çukurova University, 01330 Adana, (Turkey).
[3]INMA (CSIC-Universidad de Zaragoza), C/María de Luna 3, 50018-Zaragoza (Spain).
[4]National Institute for Materials Science, 1-2-1 Sengen, Tsukuba, Ibaraki 305-0047, Japan

Abstract
The effect of K substitution for Ca in $Bi_2Ca_{2-x}K_xCo_2O_y$ (x= 0.0, 0.05,0.075, 0.10, and 0.125) thermoelectric ceramics, produced via laser floating zone (LFZ) method, have been systematically investigated. XRD patterns are quite similar for all samples and main peaks in the patterns correspond to reflection planes of the thermoelectric phase together with small amount of secondary phases. SEM micrographs revealed well oriented grains along the growth direction, and the presence of three different contrasts, associated through EDS to different phases, namely, black (Co oxide), white (Bi poor phase) and grey ($Bi_2Ca_2Co_{1.7}O_y$ TE phase). It was also seen that the amount of secondary phases diminishes with K-increase. The room-temperature resistivity values sharply decrease from 0.75 mΩ.m for the undoped sample to 0.44 mΩ.m for the 0.05 K-doped one, increasing for higher doping. Seebeck coefficient also decreases from 190 μV/K in the pristine sample, to 160 μV/K in all the K-doped ones, at 390 K. Thermal conductivity increases with temperature up to around 250 K, decreasing at higher temperatures. Thermal conductivity at 390 K decreases from 1.1 W/K-m in the pristine sample to lower values by K-doping, reaching the minimum, 0.9 W/K-m, in the 0.125 K-doped one. As a result, the highest ZT value of has been determined in 0.05 K-doped sample, around 0.021 at 390 K.

Keywords: Texture; Microstructure; Thermoelectric oxides; Electrical properties; Figure of Merit

Corresponding author: Tel./fax:+90.322.3386080/+90.322.3386070
e-mail: ozcelik@cu.edu.tr

1. Introduction

After the discovery of the thermoelectric (TE) phenomena by Seebeck, Peltier, and Thomson, thermoelectricity has driven great attention for both scientific and technological applications. Today, the ever-increasing energy demand around the world and the accompanying environmental problems related to the emission of harmful greenhouse gases, has increased the interest in the thermoelectric phenomenon. Thermoelectric materials have wide applications in energy harvesting technologies due to their ability to convert the thermal energy into electricity or vice versa. By joining suitable n and p type materials, many functional thermoelectric modules used for power generation such as spacecraft, automobile, remote sensors, medical sensors and cooling applications such as refrigerators, optoelectronic devices, detectors, etc. have been constructed [1-5]. Because of reliability, maintenance free operations, being vibration- and noise-free and without hazardous emissions, thermoelectric generators are preferred for power generation. Thermoelectric generators are also used when durability is desired with a longer operating life under extreme conditions.

The technological performance of thermoelectric materials is often quantified through the dimensionless thermoelectric figure of merit, ZT, described as $ZT = S^2T/\rho\kappa$ where S is the Seebeck coefficient, T is the absolute temperature, ρ is the electrical resistivity and κ is the total thermal conductivity, which consists of the lattice thermal conductivity due to phononic transport, κ_L, and the electronic thermal conductivity, κ_e, due to carriers [6].

The properties sought in the desired thermoelectric materials are low electrical resistivity, high Seebeck coefficient and low thermal conductivity, to maximize ZT value. However, increasing the ZT coefficient can be a thorny issue, as the thermoelectric parameters are interdependent. The best ways to do this are increasing the power factor, identified as $S^2\sigma$ (here σ is electrical conductivity) or S^2/ρ, optimize the carrier concentration, and/or diminish the lattice thermal conductivity by creating scattering centers [6].

The first discovered CoO-based ceramic TE material is Na_xCoO_2 which possess high chemical stability at high temperatures and high thermoelectric power and electrical conductivity [7]. Therefore, this promising material has motivated researchers to explore different materials and improve their thermoelectric properties. Later on, Ca-Co-O [8], Bi-Ca-Co-O [9], and Bi-Sr-Co-O [10] p-type layered cobalt oxides and TiO-, MnO-based materials [11,12] presenting n-type behavior, were discovered. It is well-known that Co-based thermoelectric materials have a monoclinic crystal structure formed by the alternating stacking of two different a conductive and insulating layers, namely, CdI_2-type CoO_2 and rock

salt (RS) $Bi_2X_2O_4$ (X=Ca, Sr and Ba), respectively. These layers possess, generally, similar values of *a*- and *c*-axis lattice parameters and *β* angles, but different *b*-axis length, inducing a misfit throughout the *b*-direction [13,14]. This misfit structure causes an crystallographic irregularity and electrical anisotropy in the material, affecting their electrical properties and Seebeck coefficient [15].

In previous works, $Bi_2Ca_{2-x}K_xCo_2O_y$ with x=0, 0.05, 0.075, 0.10, and 0.125 thermoelectric materials were fabricated via the classical solid state route, followed by laser floating zone (LFZ) texturing, then their high temperature thermoelectric properties were, in detail, investigated [16]. In this study, the results related to the microstructure, resistivity, Seebeck coefficient, thermal conductivity and figure of merit, at low temperatures, will be presented, in order to evaluate the low temperature performances of these thermoelectric ceramics. In these conditions the fundamental properties of these materials can be more accurately determined by drastically decreasing the temperature effect. Moreover, potassium has been chosen as dopant, due to two collaborative effects: first, it decreases the charge in the RS structure and leads to the promotion of Co^{3+} to Co^{4+} in the conducting layer; and second, it decreases the misfit ratio in the crystal structure, decreasing Seebeck coefficient. Consequently, both effects are decreasing electrical resistivity, which is one of the main objectives in these materials.

2. Experimental Procedure

Polycrystalline ceramic thermoelectric samples with $Bi_2Ca_{2-x}K_xCo_2O_y$ (x= 0, 0.05, 0.075, 0.10, and 0.125; and y slightly higher than 8, depending on the Co^{4+} content) starting composition, were fabricated by classical solid-state reaction route. High purity Bi_2O_3 (98 + %, Panreac), $CaCO_3$ (98.5 %, Panreac), CoO (99.99%, Sigma-Aldrich), and K_2CO_3 (99.8 %, Panreac) commercial powders were homogenously mixed thoroughly in the desired stoichiometric ratio and ball milled in distilled water media. The suspension was dried using infrared lamps and manually ground to sunder the agglomerates. The resulting homogenous powders were prefired at 750 and 800°C for 24h twice, with intermediate grinding, in order to eliminate CO_2 from the metallic carbonates. Then, the obtained mixtures were cold isostatically formed into cylindrical shape with radius and length of 2-3mm and 100mm, respectively, under 200 MPa. Finally, for the purpose of feed usage, these rods were settled in laser floating zone system operating with Nd-YAG laser radiation, having λ=1064nm, following the procedure reported elsewhere [17]. To produce a homogeneous molten zone, the grown speed of specimens was set to 30 mm/h, with 3 rpm seed rotation while the feed

was oppositely rotated at 15 rpm. This production technique allows obtaining very dense and geometrically homogeneous fibers with about 2.5 mm diameter. In addition, to decrease the secondary phases appearing in the as-grown samples due to incongruent melting [18,19], a final heat treatment was carried out at 810°C for 24h under air atmosphere. Finally, all physical measurements have been performed on these textured and annealed samples.

The Rigaku D/max-B X-ray powder diffractometer with CuKα radiation system and a field emission scanning electron microscope (FESEM, Zeiss Merlin) attached with an EDS device have been used to characterize the structural and microstructural features of the samples. For SEM-EDS analysis, the rods (specimens) were hot embedded in conductive resin and longitudinal polished sections were prepared by grounding to reach their centers and finally polished with diamond paste. Archimedes' method was used to obtain the density of samples, taking 6.8 g/cm^{3}as theoretical density [19]. Quantum Design PPMS system operating between 4.2–390 K was used to, simultaneously, measure the resistivity (*ρ)*, thermal conductivity *(κ)* and Seebeck coefficient (*S)*. For this purpose, a sample is subjected to a thermal pulse, under high vacuum, and its temperature and voltage responses are recorded. Fitting algorithms based on a model of the thermal circuit extract a sample's thermal conductance and Seebeck coefficient from these curves, and a resistance measurement is executed immediately after. ZT is automatically calculated as well, and can be evaluated across the full range of temperature and field afforded by the PPMS. The magnetization against temperature and applied field (hysteresis) were measured by using a Dyne-cool PPMS (Quantum Design) magnetometer. The magnetic hysteresis data have been collected between –5 and +5 Tesla external applied fields, and magnetization measurements have been made under 20 Oersted dc external field between 5-300 K, in zero field cooled (ZFC) mode. In following sections, the samples with x= 0, 0.05, 0.075, 0.10, and 0.125 will be labeled as A, B, C, D and E, respectively.

3. Results and Discussion:

XRD patterns of polycrystalline powder of $Bi_2Ca_{2-x}K_xCo_2O_y$ fibers are presented in Fig. 1. It is obviously seen that most of the peaks represent the definite diffraction *(00l)* planes corresponding to $Bi_2Ca_2Co_2O_y$ thermoelectric phase. This points out the formation of almost single phase compound. Furthermore, no significant secondary phase peaks can be observed, indicating potassium (K) incorporates successfully into the main structure. Moreover, no shift with K-content is observed in the main peaks, probably due to the low amount of K in the samples associated to a possible K evaporation [20,21]. Additionally, despite the incongruent

melting of these compounds, very low amount of secondary phases could be identified, labeled as *, which correspond to an orthorhombic $Bi_6Ca_4O_{13}$ secondary phase [22], in agreement with previous works [23].

It is already reported that the LFZ system improves the grain orientation in the materials causing an improvement of TE-parameters [16,24]. Lotgering factor (LF) is given with $LF = (P-P_0)/(1-P_0)$ formula, in which P is the sum of the peak intensities of preferred orientation, and P_0 is the sum of the peaks related to the randomly-oriented grains [25,26]. The calculated LF values for A, B, C, D, and E samples are 0.742, 0.778, 0.790, 0.789, and 0.781, respectively. As can be found, LF value increases with increasing K-substitution up to ~~0.075K~~ sample C (x=0.075) and then it shows a slight decrease. These phenomena point out to the effect of secondary phases in the structure producing significant variations at the intensity of peaks. On the other hand, the improvement of grain orientation is due to the presence of K_2CO_3 in the precursor compounds, which decreases the melting point of the compound. Consequently, the radial thermal gradient at the solidification interface is decreased, reducing the misorientation of grains, as already observed through other approaches in similar materials [27].

To see better the surface morphology and to identify the elemental composition of phases, the representative SEM micrographs taken with secondary electrons of all samples are presented in Fig. 2. As can be seen all micrographs present three different contrasts, with different compositions, as determined via EDS technique: Black (Co oxide), white (Bi poor phase) and grey ($Bi_2Ca_2Co_{1.7}O_y$ TE phase). The EDS results obtained in the different contrasts in all samples are summarized in Table 1 for clarity. As it can be observed, there is a range in compositions depending on the measured region and samples. However, the most important comment is related to the potassium presence in the doped samples, which is below the detection limit for K-content up to 0.075, and below the nominal one for higher content. These results confirm, in spite that they are only semi-quantitative, a partial evaporation of potassium during the processing and its presence in the thermoelectric phase. These micrographs also shown that the proportion of secondary phases reduces by increasing K-content, which induces larger grain sizes and better orientation, as in observed through XRD mentioned above.

The low temperature resistivity graphs of $Bi_2Ca_{2-x}K_xCo_2O_y$ samples measured in the range of 5 and 390K are presented in Fig. 3. All samples exhibit the same kind of behavior similar to normal semiconductors. Resistivity begins to decrease from low temperature region towards high ones ($d\rho/dt<0$), presenting very broad minimum at around 75 K, named metal-insulator-

transition (T_{min}) temperature. Later on, all samples show very slow increase at higher temperatures. Moreover, the values are decreased with increment of K-substitution, similar to the previous reports [28,29]. By evaluating these results, it can be concluded that Ca^{2+} is replaced by K^{+} inducing a decrease of the oxidation state of RS layer, and a promotion of Co^{3+} to Co^{4+} in the conducting one, to maintain the electrical neutrality. This result is confirmed by previous observations in melt-textured materials, which shows that laser processing leads to the formation of unusually large oxygen vacancies [30], avoiding the formation of further ones by K-doping. Hence, the resistivity values diminish by increasing K-substitution due to the increase of charge carrier concentration and grain orientation. As it has been already mentioned in the introduction, the crystal structure is formed by two layers, leading to large anisotropy, which favors the grain growth along the ab-planes. Moreover, these planes are the conducting ones and the current transport is enhanced when these grains are aligned with small angles between their c-axis, as shown in similar systems [31]. The obtained room-temperature resistivity values for A, B, C, D, and E samples are 0.75, 0.44, 0.61, 0.62 and 1.03 mΩ.m, respectively.

For deeply analyzing the resistivity results, the Variable Range Hopping (VRH) [32] model is used. In this model the resistivity is given by,

$$\rho(T) = \rho(0)\ exp\ (T_0/T)^{1/3} \qquad (1)$$

in which $\rho(0)$ is a pre-expontial factor, T_0 is the temperature identified by $T_0=8/[\pi k_B N(\varepsilon_F) l_v^2]$, where $N(\varepsilon_F)$ is the density of localized states at Fermi level, l_v is the localization length and k_B is Boltzmann constant [33]. T_0 value is calculated from the slope of $ln\rho(T)$ versus $T^{-1/3}$ plots given in Fig. 4, as 40.30, 26.90, 26.86, 27.34, and 28.89 K for A, B, C, D, and E samples, respectively. At a first glance, T_0 values reduce with increasing of K-substitution up to sample C (x=0.075), then slightly increase. This behavior points out an increment of localization length, l_v, concerning to the weak carrier localization and the increment of mobility.

The holes jumping occurs to lower energy levels rather than higher energy neighboring ones, in the low temperature range. Hence the Variable Range Hopping theory is used in the low temperatures if thermally activated energy is insufficient for jumping the holes into the nearest higher-energy regions. If the carriers can get enough energy with increasing temperature in order to stimulate hole carriers, instead of VRH model, thermally activated conduction (TAC) theory is preferred [34].

According to TAC model, the resistivity is given by:

$$\frac{1}{\rho} = \mu(T)\, exp\left(-\frac{E_0}{k_B}\right) \quad (2)$$

If this formula is arranged as;

$$ln\rho = \frac{E_0}{k_B}T^{-1} - ln\mu = AT^{-1} + B \quad (3)$$

where k_B is the Boltzmann constant, $\mu(T)$ is the mobility of the carriers, E_0 is the activation energy due to the spin density wave (SDW) setting at Fermi surface, and A ($=E_0/k_B$) and B ($=-ln\mu$) are fitting parameters. From this formula, the low temperature resistivity data are plotted in Fig. 5. For the samples A, B, C, D, and E, E_0 activation energies are deduced by using the slope of curves as 12.5, 7.9, 8.2, 8.1, and 8.1 meV, respectively.

As it can be seen, E_0 values slightly fluctuate around 8 meV for K-substituted samples, except pure one. This may be due to the K^{+1} for Ca^{+2} substitution, which leads to a structural distortion. This distortion phenomenon may affect the structure of the spin density wave propagating in the CoO_2 plane. To understand the origin of physical fact, the selected area electron diffraction (SAED) experiment has been applied [35]. It has been concluded that some secondary phases possess some imperfections in the atomic structure of $Bi_2Ca_2Co_2O_y$ inducing low crystal symmetry.

Fig. 6 shows the Seebeck coefficient evolution with temperature for all samples. All graphs of Seebeck coefficient are positive indicating the domination of hole carriers. At low temperatures, the Seebeck coefficient of all samples starts to linearly raise with temperature up to approximately 100K, then all data related to K-doped samples arrive to a plateau-like region around room temperature, finally they slightly tend to increase toward to high temperatures. While the value of Seebeck coefficient of pristine sample is around 190 μV/K, for K-doped samples it reaches 160 μV/K at 390 K. It can be concluded that the Seebeck coefficient is affected by the K-doping, which modifies the misfit ratio in the crystal structure, as previously demonstrated [36].

As a result, due to distortion of atomic structure, the Co^{3+} spin state is driven from high spin state to low spin state then, the misfit ratio directly regulates the Co^{3+} amount. Consequently, this regulation strongly affects the Seebeck coefficient. On the other hand, since the Seebeck coefficient (S) values are nearly interdependent of temperature around room temperature, S can follow the so-called modified Heike's formula proposed by Koshibae et. al [37]

$$S = -\frac{k_B}{|e|} ln\left(\frac{1}{6}\frac{x}{1-x}\right) \quad (4)$$

where e is the charge of electron, k_B is the Boltzmann constant, and x is the fraction of Co^{+4} ions. By using this formula and the fraction of Co^{+4} ions are calculated and presented in Table 2. From the obtained values, all K-doped samples have higher Co^{+4} concentrations which can be a sign of promotion of Co^{3+} to Co^{4+} as previously discussed in electrical resistivity versus temperature results.

In Fig. 7, thermal conductivity graphs as a function of temperature are plotted with respect to temperature. The thermal conductivity value of pristine sample is higher than those of all K-substituted samples. All $\kappa(T)$ values linearly increase as temperature rises, reach a maximum around 200 K, and finally drop at higher temperatures.

Thermal conductivity has a phonon and carrier thermal conductivity components, expressed by the formula [38];

$$\kappa(T) = \kappa_{ph}(T) + \kappa_{ch}(T) \qquad (5)$$

The carrier thermal conductivity component is obtained via Wiedemann-Franz formula given by $\kappa_{ch}(T)=LT/\rho$. Here, L is Lorenz number ($2.45*10^{-8}$ V^2/K^2), ρ is the electrical resistivity, and T is the absolute temperature. For the samples A, B, C, D, and E, κ_{ch} values, at room temperature, were obtained as 1.21, 1.07, 1.04, 1.1, and 1.0 $WK^{-1}m^{-1}$, respectively.

The figure of merit, ZT, values of samples are calculated by using the formula $ZT = S^2T/\rho\kappa$, and presented, as a function of temperature, in Fig. 8. The largest ZT value belongs to the B sample (x=0.05) as 0.0125 at 300 K, which is slightly higher than the reported values for melt quenched samples (0.010) [39].

As it is known that the presence of magnetic atoms in oxide thermoelectric enhances their thermoelectric characteristics by increasing the thermoelectric power since the thermoelectric quantities are oversensitive to very small modifications of magnetic properties. Hence, we have performed the magnetic experiments on the samples to find out their possible usage for thermoelectric cooling. In addition, magnetic measurements can give an indirect knowledge about valence states of Co-ions in these systems [40]. To be more specific, In CdI_2-type CoO_2 layer, 3d orbitals of Co-ions are split into the triply degenerate t_{2g} orbitals and the doubly degenerate e_g orbitals with energy gap called the crystal-field splitting energy Δ between them. The Co^{+3} and Co^{+4} ions can have low spin (LS), intermediate spin (IS), and high spin (HS) as a result of competition between crystal-field splitting energy and the Hund coupling energy, K [34]. In each spin configurations, Co^{+4} ions have higher magnitude of spin, S [37]. To have idea about spin states of Co ions, magnetization versus temperature and magnetizations versus magnetic field measurements were performed. Magnetization values with respect to the temperature are plotted in Fig. 9. As shown in the figure magnetization

values at room temperature increases with K-doping. This behaviour can be a sign of a promotion of non-magnetic Co^{3+} (lower magnitude of spin) to magnetic Co^{4+} (higher magnitude of spin) [37]. The graphs of all samples exhibit Curie-Weiss paramagnetic behaviour in the high temperature region. Then, the magnetization values start to sharply increase around T=50 K. For characterizing this anomaly, Curie-Weiss law has been used:

$$\frac{1}{\chi_{DC}} = \frac{H}{M} = \frac{T-\theta}{C} \qquad (6)$$

Here, C and θ are Curie constant and the Curie-Weiss temperature, respectively.
When plotting $1/\chi$ versus T, as seen in Fig. 10, Curie-Weiss temperature and Curie constant are obtained from the interception of temperature axis and the slope of fitting line, respectively. The obtained values are presented in Table 1. As it can be seen, $\boldsymbol{\theta}$ values are negative, suggesting that antiferromagnetic behavior prevails in the low temperature region. Higher θ values in K-doped samples indicate that antiferromagnetic behavior is suppressed by K-substitution as in the case of Pb-substituted Bi–Ca–Co–O misfit-layer cobaltites [41]. As it is well-known that the Curie temperature is affected by the alignment of magnetic moments in the material. If the magnetic moments in the material are parallel with each other the Curie temperature increases and if perpendicular, the Curie temperature decreases. Depending on the variation of the Curie temperature, the Curie constant also changes. As can be seen in Table-1, it increases up to C (x=0.075) sample, then starts to decrease due to the magnetic ordering in the matrix.

The effective magnetic moment, μ_{eff}, of samples was found by using the equation;

$$\mu_{eff} = \left[\frac{3k_B C M_w}{N}\right]^{1/2} \qquad (7)$$

where, M_w is the molecular weight of sample, N is Avogadro number ($6.02\text{x}10^{23}$ atoms/mol), k_B is Boltzmann constant ($1.38\text{x}10^{-16}$ erg/K), and C is Curie constant. According to the calculated values which fluctuate around 2 for the K-doped samples displayed in Table-1. All K-doped samples have slightly higher C and μ_{eff} showing that increase of number of Co^{4+} ions and decrease of impurity phase in the system [42].

Finally, magnetic hysteresis graphs measured at T=10 K are presented in Fig. 11. These results show that all curves are quite similar and very narrow hysteretic behavior is observed at T=10K in K-doped samples as seen in inset of Fig.11, showing that antiferromagnetic interaction slightly degrades with K-doping in accordance with higher Curie-Weiss temperature in K-content samples.

4. Conclusion

In this study, $Bi_2Ca_{2-x}K_xCo_2O_y$ (x= 0.0, 0.05, 0.075, 0.10, and 0.125) thermoelectric fibers were produced by a texturing process via LFZ technique. XRD patterns have shown that major peaks are related to *(00l)* reflections of $Bi_2Ca_2Co_2O_y$ TE-phase, independently of K-content. The obtained Lotgering factors showed an increase of grain orientation up to x=0.075 potassium (K) content. From the SEM micrographs, it was observed that the amount of secondary phases has diminished by increasing K-content, resulting in larger grains and better grain orientation. The room-temperature resistivity values decreased with K-doping up to x = 0.05, increasing for further doping. By using variable range hopping model, T_0 values were shown to decrease with K-addition. Moreover, from thermally activated conduction (TAC) model has been found that E_0 activation energies were also decreased. While Seebeck coefficient of pristine sample was around 190 μV/K, for K-doped samples it decreased to 160 μV/K, at 390 K. Thermal conductivity was monotonously decreased with K-content at room temperature. The largest ZT value at 300K (x=0.125) has been determined in the x=0.05 sample. The magnetic results demonstrated that antiferromagnetic interactions were dominant in the low temperature region in all K-substituted samples.

Acknowledgements

This study was carried out within the scope of Cukurova University Scientific Research Projects Unit FBA-2021-14163, FBA-2020-12784, FBA-2022-14414. The authors wish to thank the Spanish MINECO-FEDER (MAT2017-82183-C3-1-R), and Gobierno de Aragón (Research Group T54-20 R) for funding. The authors wish to acknowledge the use of Servicio General de Apoyo a la Investigación-SAI, Universidad de Zaragoza.

References:

[1] I. Caplain, F. Cazier, H. Nouali, A. Mercier, J. C. Dechaux,V. Nollet, R. Joumard, J.M. Andre, R. Vidon, Atmospheric Environment 40 (31) (2006) 5954.

[2] H. Alam, S. Ramakrishna, A review on the enhancement of figure of merit from bulk to nano-thermoelectric materials, Nano Energy 2, (2013) 190.

[3] D.M. Rowe, International Journal of Innovations in Energy Systems and Power 1 (1) (2006).

[4] G. Jeffrey Snyder, The Electrochemical Society Interface (2008) 54–56.

[5] D. Zhao, G. Tan, A review of thermoelectric cooling: Materials, modeling and Applications, App. Ther. Eng. 66 (2014) 15.

[6] D.M. Rowe, in: D.M. Rowe (Ed.), Thermoelectrics Handbook: Macro to Nano, 1st edn, CRC Press, Boca Raton, FL, 2006, pp. 1–3

[7] M.H. Elsheikh, D.A.Shnawah, M.F.M.Sabri, S.B.M.Said, M.H.Hassan, M.B.A. Bashir, M.Mohamad, A review on thermoelectric renewable energy: principle parameters that affect their performance, Renew.Sust. Energy Rev30 (2014) 337.

[8] S. Li, R. Funahashi, I. Matsubara, K. Ueno, H. Yamada, High temperature thermoelectric properties of oxide $Ca_9Co_{12}O_{28}$, J. Mater. Chem. 9, (1999)1659.

[9] A. Maignan, S. Hebert, M. Hervieu, C. Michel, D. Pelloquin, D. Khomskii, Magnetoresistance and magneto thermopower properties of Bi/Ca/Co/O and Bi(Pb)/Ca/Co/O misfit layer cobaltites J. Phys.:Condens. Matter 15, 2711 (2003)

[10] R. Funahashi, I. Matsubara, A. Sodeoka, Thermoelectric properties of Bi2Sr2Co2Ox polycrystalline materials Appl. Phys. Lett. 76, (2000) 2385.

[11] H. Wang, C.L. Wang, Thermoelectric properties of Yb-doped $La_{0.1}Sr_{0.9}TiO_3$ ceramics at high temperature, Ceram. Int. 39 (2013) 941–946.

[12] Y.H. Zhu, W.B. Su, J. Liu, Y.C. Zhou, J. Li, X. Zhang, Y. Du, C.L. Wang, Effects of Dy and Yb co-doping on thermoelectric properties of $CaMnO_3$ ceramics, Ceram. Int. 41 (2015) 1535–1539.

[13] Y. Miyazaki, Crystal structure and thermoelectric properties of the misfit-layered cobalt oxides, Solid State Ion. 172 (2004) 463.

[14] H. Leligny, D. Grebille, O. Perez, A.C. Masset, M. Hervieu, B. Raveau, A five-dimensional structural investigation of the misfit layer compound $[Bi_{0.87}SrO_2]_2[CoO_2]_{1.82}$, Acta Cryst. B 56 (2000) 173.

[15] A. Sotelo, Sh. Rasekh, M. A. Torres, M. A. Madre, J. C. Diez, Preparation of high performance $Bi_2Sr_2Co_{1.8}O_x$ thermoelectric materials from nanosized precursors, Adv. Appl. Ceram., 116/ 7, (2017) 383.

[16] C. Özçelik, T. Depci, M. Gürsul, G. Çetin, B. Özçelik, M. A. Torres, M. A. Madre, A. Sotelo, Tuning thermoelectric properties of $Bi_2Ca_2Co_2O_y$ through K doping and laser floating zone processing, Solid State Sciences 120 (2021) 106732

[17] A. Sotelo, E. Guilmeau, M. A. Madre, S. Marinel, J. C. Diez, M. Prevel, Fabrication and properties of textured Bi-based cobaltite thermoelectric rods by zone melting, J. Eur. Ceram. Soc. 27 (2007) 3697-3700.

[18] S.h. Rasekh, F.M. Costa, N.M. Ferreira, M.A. Torres, M.A. Madre, J.C. Diez, A. Sotelo, Use of laser technology to produce high thermoelectric performances in $Bi_2Sr_2Co_{1.8}O_x$, Mater. Design 75 (2015) 143.

[19] E. Combe, R. Funahashi, T. Barbier, F. Azough, R. Freer, Decreased thermal conductivity in $Bi_2Sr_2Co_2O_x$ bulk materials prepared by partial melting, J. Mater. Res. 31 (2016) 1296.

[20] R. L. Lehman, J. S. Gentry, N. G. Glumac, Thermal stability of potassium carbonate near its melting point, Thermochim. Acta 316 (1998) 1–9.

[21] K. Sugiura, M. Yamauchi, K. Tanimoto, Y. Yoshitani, Evaluation of volatile behaviour and the volatilization volume of molten salt in DIR-MCFC by using the image measurement technique, J. Power Sources 145 (2005) 199–205.

[22] Standard ICSD card nº 01-080-1123.

[23] Sh. Rasekh, M. A. Madre, J. C. Diez, E. Guilmeau, S. Marinel, A. Sotelo, Effect of Pb substitution on the thermoelectrical properties of textured $Bi_2Ca_2Co_{1.7}O_x$ ceramics prepared by a polymer solution method, Bol. Soc. Esp. Ceram. V. 49 (2010) 371-376.

[24] G. Çetin, B. Özçelik, M. Gürsul, M.A. Torres, M.A. Madre, A. Sotelo, Effect of annealing and potassium substitution on the thermoelectric and magnetic properties of directionally grown Bi2Sr2Co2O*y* ceramics, Bol. Soc. Esp. Ceram. V., 59 (2020) 121

[25] A. Sotelo, Sh. Rasekh, G. Constantinescu, M.A. Torres, M.A. Madre, J.C. Diez Improvement of textured $Bi_{1.6}Pb_{0.4}Sr_2Co_{1.8}O_x$ thermoelectric performances by metallic Ag additions, Ceramics International 39 (2013) 1597–1602.

[26] M. Kato, Y. Goto, K. Umehara, K. Hirota, I. Terasaki, Synthesis and physical properties of Bi–Sr–Co–oxides with 2D-triangular Co layers intercalated by iodine, Physica B 378–380 (2006) 1062–1063.

[27] M. F. Carrasco, R. A. Silva, R. F. Silva, V. S. Amaral, F. M. Costa, Critical current density improvement in BSCCO superconductors by application of an electric current during laser floating zone growth, Physica C 460-462 (2007) 1347-1348.

[28] E. Guilmeau, M. Pollet, D. Grebille, D. Chateigner, B. Vertruyen, R. Cloots, and R. Funahashi, Mater. Res. Bull. 43, (2008) 394.

[29] J.C. Diez, Sh. Rasekh, M.A. Madre, E. Guilmeau, S. Marinel, A. Sotelo, Improved Thermoelectric Properties of Bi-M-Co-O (M = Sr, Ca) Misfit Compounds by Laser Directional Solidification, Journal of Elect. Mater., 39/9, (2010), 1601.

[30] A. Sotelo, E. Guilmeau, M. A. Madre, S. Marinel, S. Lemonnier, J. C. Diez, $Bi_2Ca_2Co_{1.7}O_x$ thermoelectric ceramics textured by laser floating zone method, Bol. Soc. Esp. Ceram. V. 47 (2008) 225-228.

[31] B. Hensel, J.-C. Grivel, A. Jeremie, A. Perin, A. Pollini, R. Flukiger, A model for the critical current in $(Bi,Pb)_2Sr_2Ca_2Cu_3O_x$ silver-sheathed tapes: The role of small-angle c-axis grain boundaries and of the texture, Physica C 205 (1993) 329-337.

[32] H. Itahara, C. Xia, J. Sugiyama, T. Tani, Fabrication of textured thermoelectric layered cobaltites with various rock salt-type layers by using β-$Co(OH)_2$ platelets as reactive templates, J. Mater. Chem. 14 (2004) 61.

[32] N.F. Mott, E.A. Davis, Electronic Processes in Non-Crystalline Materials, Clarendon Press, London, 1971.

[33] Y. Huang, B. Zhao, R. Ang, S. Lin, Z. Huang, S. Tan, Y. Liu, W. Song, Y. Sun, Enhanced thermoelectric performance and room-temperature spin-state transition of Co^{4+} ions in the $Ca_3Co_{4-x}Rh_xO_9$ system, J. Phys. Chem. C 117 (2013) 11459.

[34] N. Sun, S. T. Dong, B.B. Zhang, Y.B. Chen, J. Zhou, S.T.Zhang, Z.B. Gu,S.H. Yao, Y.F. Chen, Intrinsically modified thermoelectric performance of alkaline-earth isovalently substituted $[Bi_2AE_2O_4][CoO_2]_y$ single crystals, J.Appl.Phys.114 (2013) 043705.

[35] A. Maignan, D. Pelloquin, S. Hebert, Y. Klein, M. Hervieu, Thermoelectric Power In Misfit Cobaltites Ceramics: Optimization By Chemical Substitutions, Bol. Soc. Esp. Ceram. V. 45 (2006) 122-125.

[36] W. Koshibae, K. Tsutsui, S. Maekawa, Thermopower in cobalt oxides, Phys. Rev. B 62 (2000) 6869–6872.

[37] Y. Wang, Y. Sui, X.J. Wang, W.H. Su, X.Y. Liu, Enhanced high temperature thermoelectric characteristics of transition metals doped $Ca_3Co_4O_{9+\delta}$ by cold high pressure fabrication, J. Appl. Phys. 107 (2010) 033708.

[38] J. Lingner, R. Funahashi, E. Combe, M. Letz, G. Jakob, Thermoelectric sintered glass-ceramics with a $Bi_2Sr_2Co_2O_x$ phase, Appl. Phys. A 120 (2015) 59.

[39] E. Iguchi, S. Katoh, H. Nakatsugawa, F. Munakata, Thermoelectric Properties (Resistivity and Thermopower) in $(Bi_{1.5}Pb_{0.5}Ca_{2-x}M_xCo_2O_{8-\delta}$ ($M=Sc^{3+}$, Y^{3+}, or La^{3+}), Journal of Solid State Chemistry 167 (2002) 472–479

[40] Y. Tanaka, T. Fujii, M. Nakanishi, Y. Kusano, H. Hashimoto, Y. Ikeda, J. Takada, Systematic study on synthesis and structural, electrical transport and magnetic properties of Pb-substituted Bi–Ca–Co–O misfit-layer cobaltites, Solid State Communications, 141, 3 (2007) 122-126.

[41]. S. Altin, A. Bayri, S. Demirel, M.A. Aksan, Thermal conductivity and magnetic properties of the B substituted $Ca_3Co_4O_9$, Current Applied Physics, 14, 4 (2014) 590-595

Table 1. Elemental cationic composition (in at. %) of the different contrasts observed in the SEM micrographs, obtained through EDS analysis.

Contrast	**Bi**	**Ca**	**Co**	**K**	**O**
Black	----	----	39.63-41.22	----	60.37-58.78
White	25.99-21.35	16.16-11.47	----	----	57.85-67.18
Grey	15.22-12.04	14.71-13.60	12.60-11.57	0.0-0.62	57.55-61.83

Table 2. Magnetic parameters for all K-doped samples

Samples	Curie-Weiss Temp. θ (K)	Curie Const. C (emuK/g)×10^{-6}	Eff. Moment $\mu_{eff}(\mu_B)$
0 K	-73,7	4,74	0,19
0.05 K	-26,3	8,36	0,20
0.075 K	-25,2	12,75	0,23
0.100 K	-20,9	9,16	0,22
0.125K	-18,3	8,53	0,23

FIGURE CAPTIONS

Figure 1. XRD patterns of $Bi_2Ca_{2-x}K_xCo_2O_y$ samples. Diffraction planes identify the peaks associated to the thermoelectric phase, while ★ corresponds to Co-free secondary phase.

Figure 2. Representative SEM micrographs of $Bi_2Ca_{2-x}K_xCo_2O_y$ samples. (a) A, (b) B, (c) C, (d) D, and (e) E. White, black and grey contrasts correspond to Bi poor phase, CoO, and TE phase similar to $Bi_2Ca_2Co_{1.7}O_y$, respectively.

Figure 3. Temperature dependence of electrical resistivity for $Bi_2Ca_{2-x}K_xCo_2O_y$ samples

Figure 4. $ln\ \rho$- $T^{-1/3}$ plots for $Bi_2Ca_{2-x}K_xCo_2O_y$ samples

Figure 5. $ln\ \rho$- T^{-1} plots for $Bi_2Ca_{2-x}K_xCo_2O_y$ samples

Figure 6. Temperature dependence of Seebeck coefficient for $Bi_2Ca_{2-x}K_xCo_2O_y$ samples

Figure 7. Temperature dependence of thermal conductivity for $Bi_2Ca_{2-x}K_xCo_2O_y$ samples

Figure 8. ZT evolution with respect to temperature for $Bi_2Ca_{2-x}K_xCo_2O_y$ samples

Figure 9. Temperature dependence of magnetization for $Bi_2Ca_{2-x}K_xCo_2O_y$ samples

Figure10. Normal and inverse susceptibility versus temperature graphs for the pristine sample

Figure 11. M-H plot of $Bi_2Ca_{2-x}K_xCo_2O_y$ samples, measured at T=10 K

Figure 1

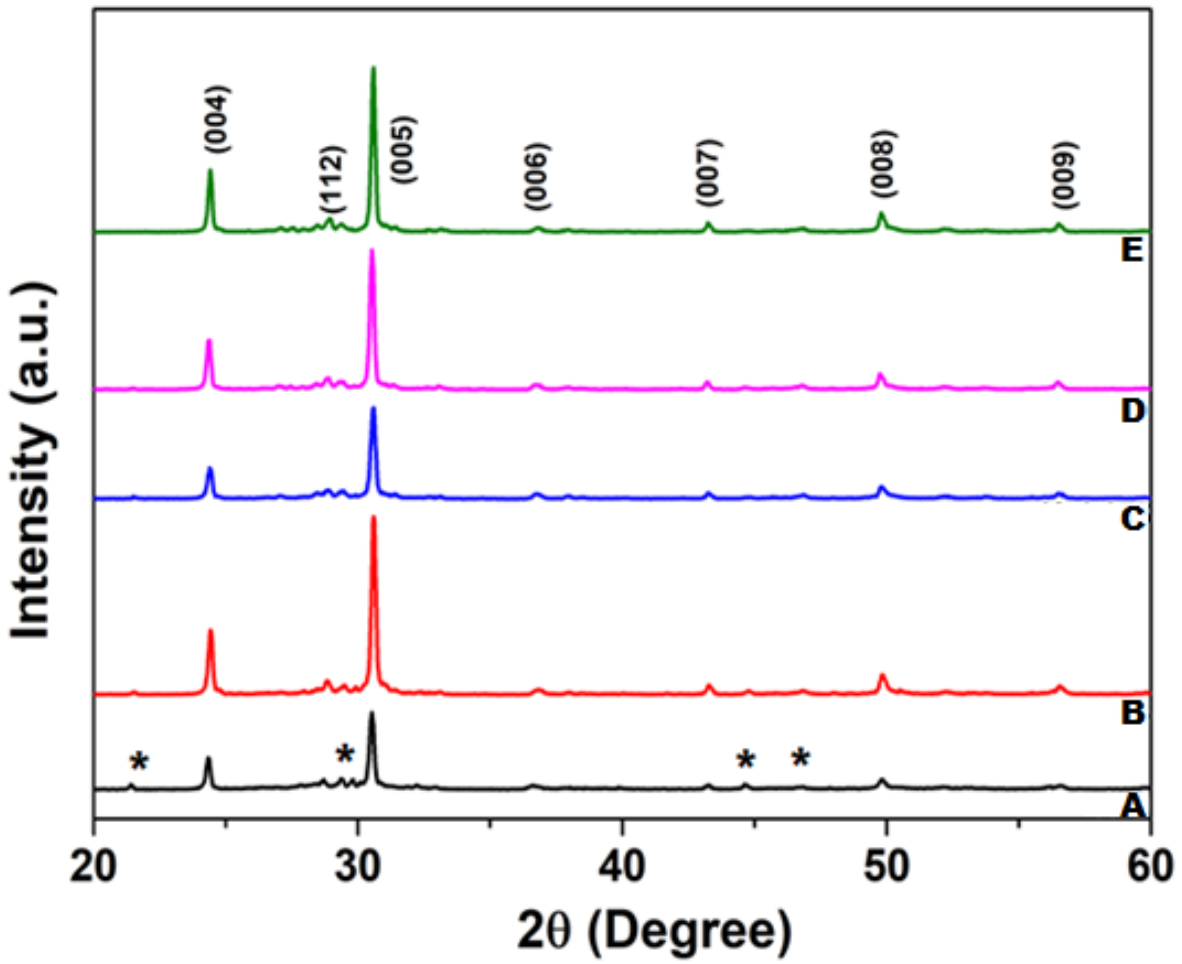
(004)
(112)
(005)
(006)
(007)
(008)
(009)
E
D
C
B
A
*
*
*
*
Intensity (a.u.)
20
30
40
50
60
2θ (Degree)

Figure 2

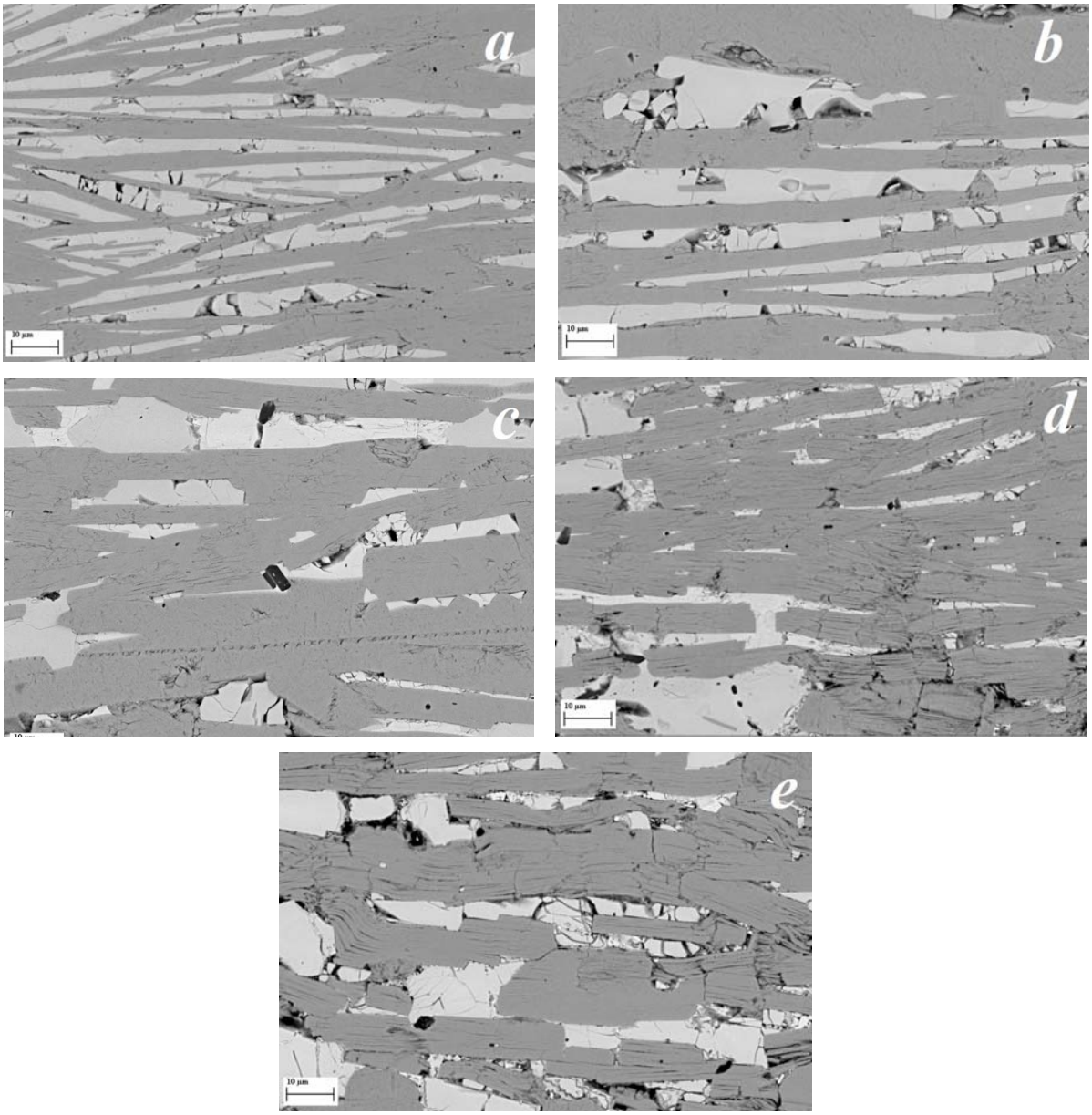

Figure 3

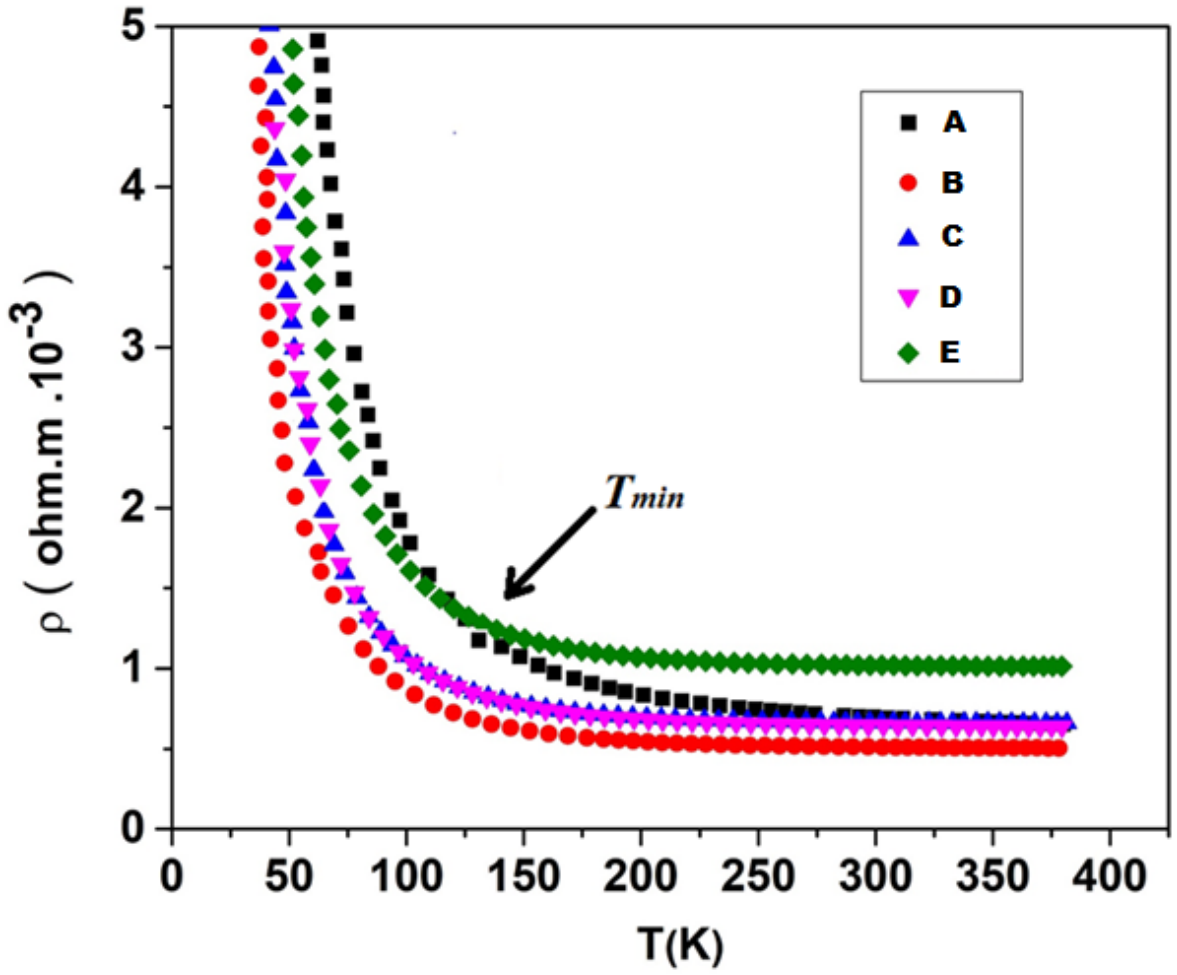

Figure 4

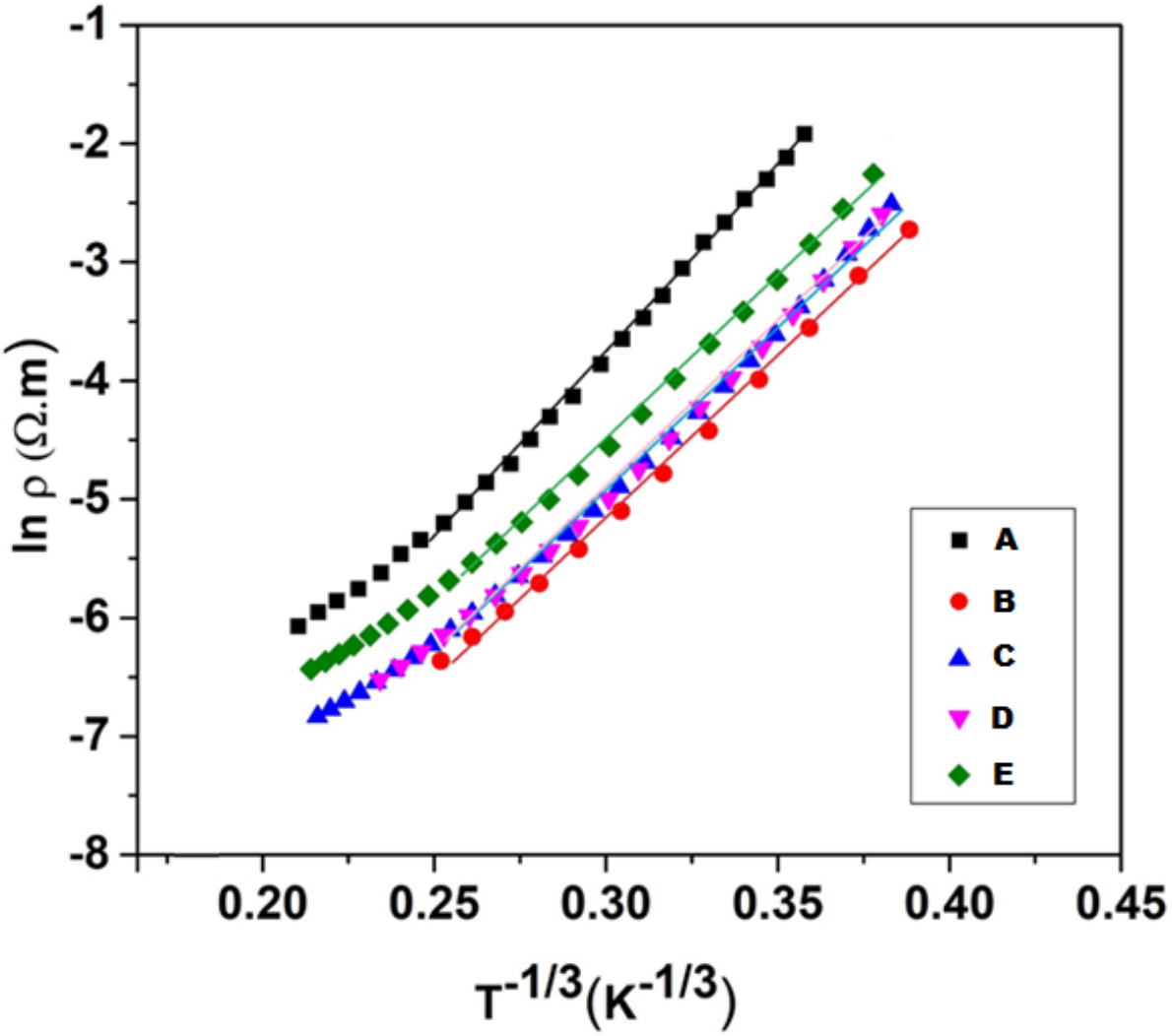

Figure 5

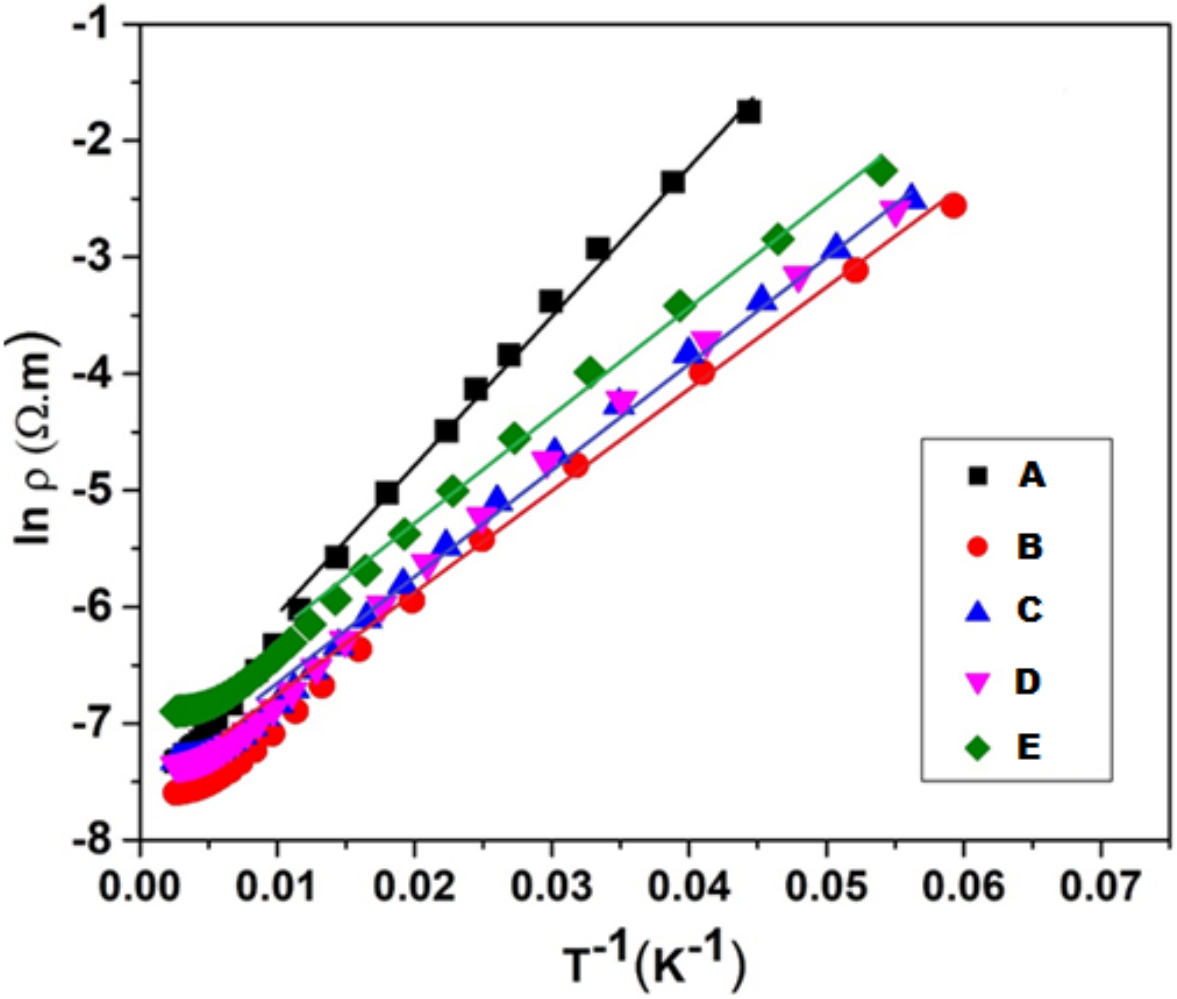

Figure 6

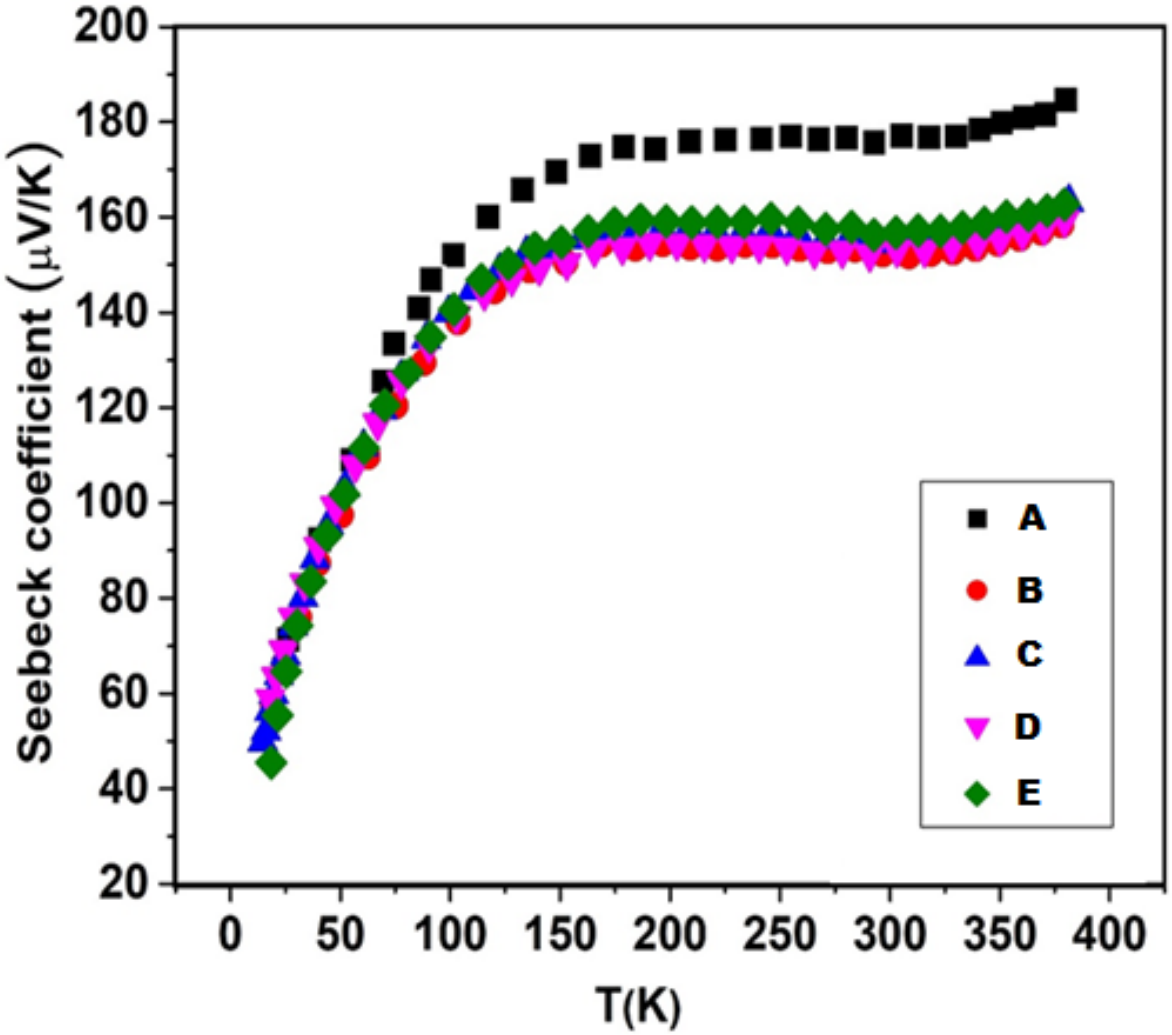

Figure 7

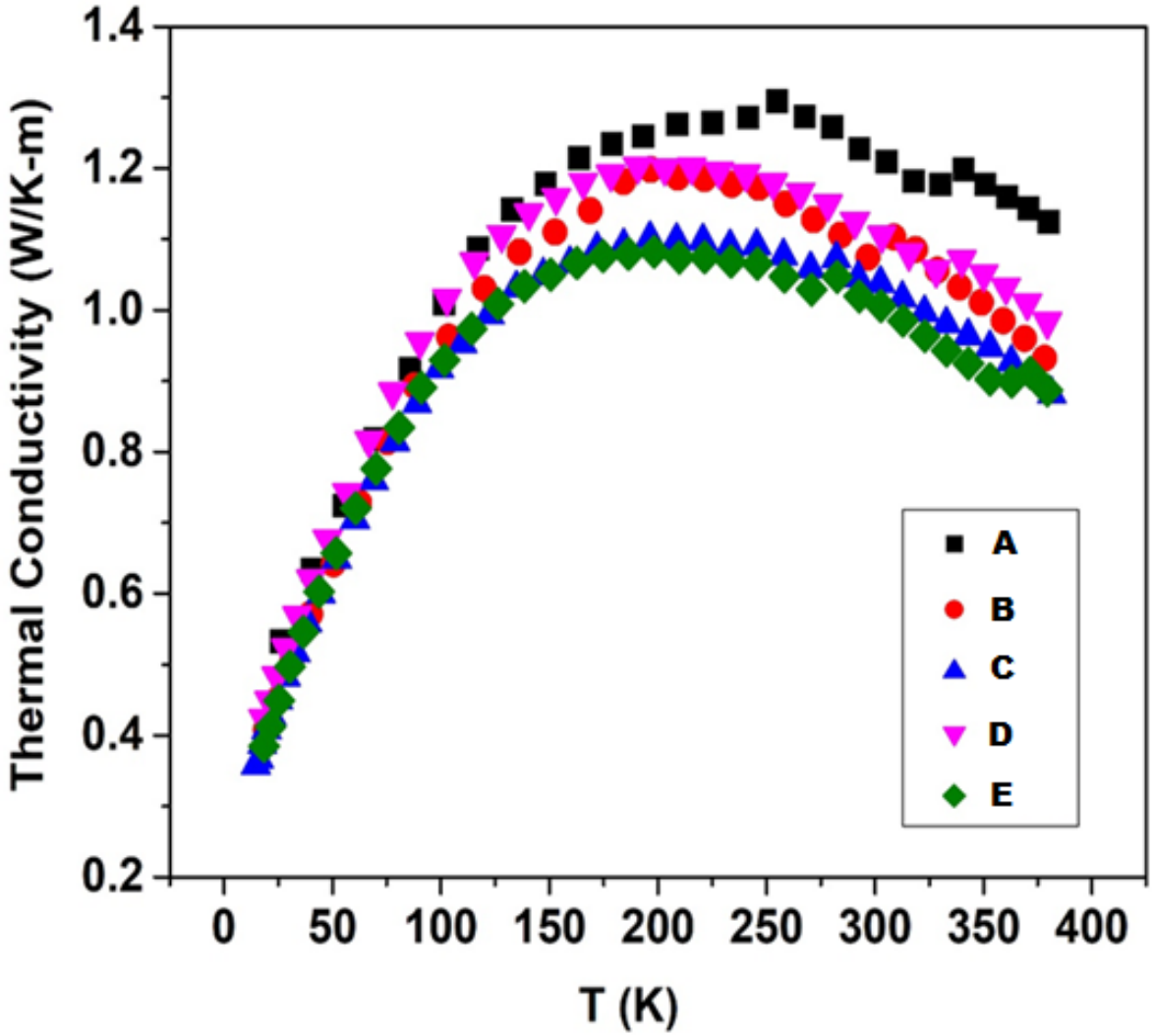
Thermal Conductivity (W/K-m)
1.4
1.2
1.0
0.8
0.6
0.4
0.2
0
50
100
150
200
250
300
350
400
T (K)
A
B
C
D
E

Figure 8

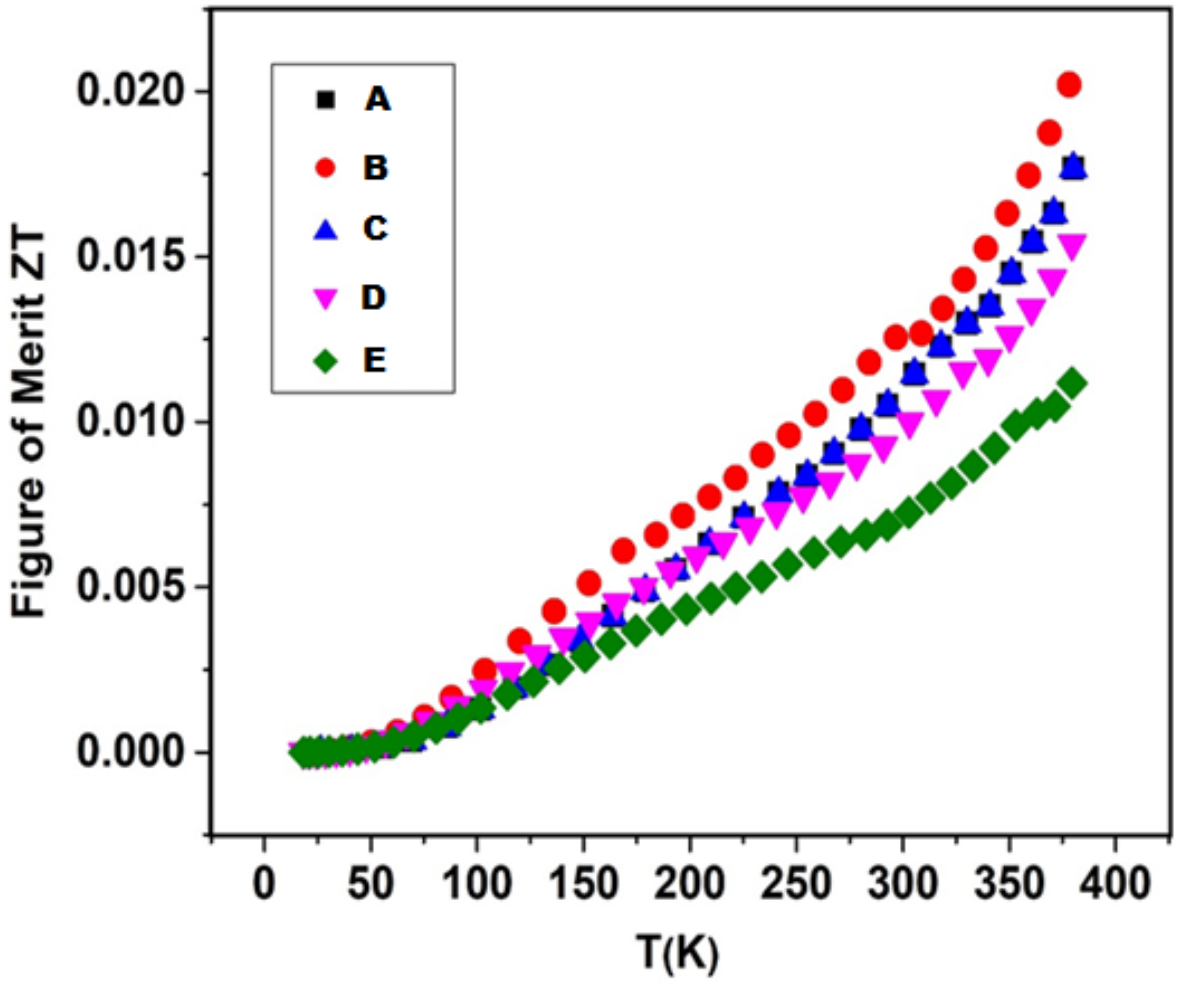
Figure of Merit ZT
0.020
0.015
0.010
0.005
0.000
A
B
C
D
E
0
50
100
150
200
250
300
350
400
T(K)

Figure 9

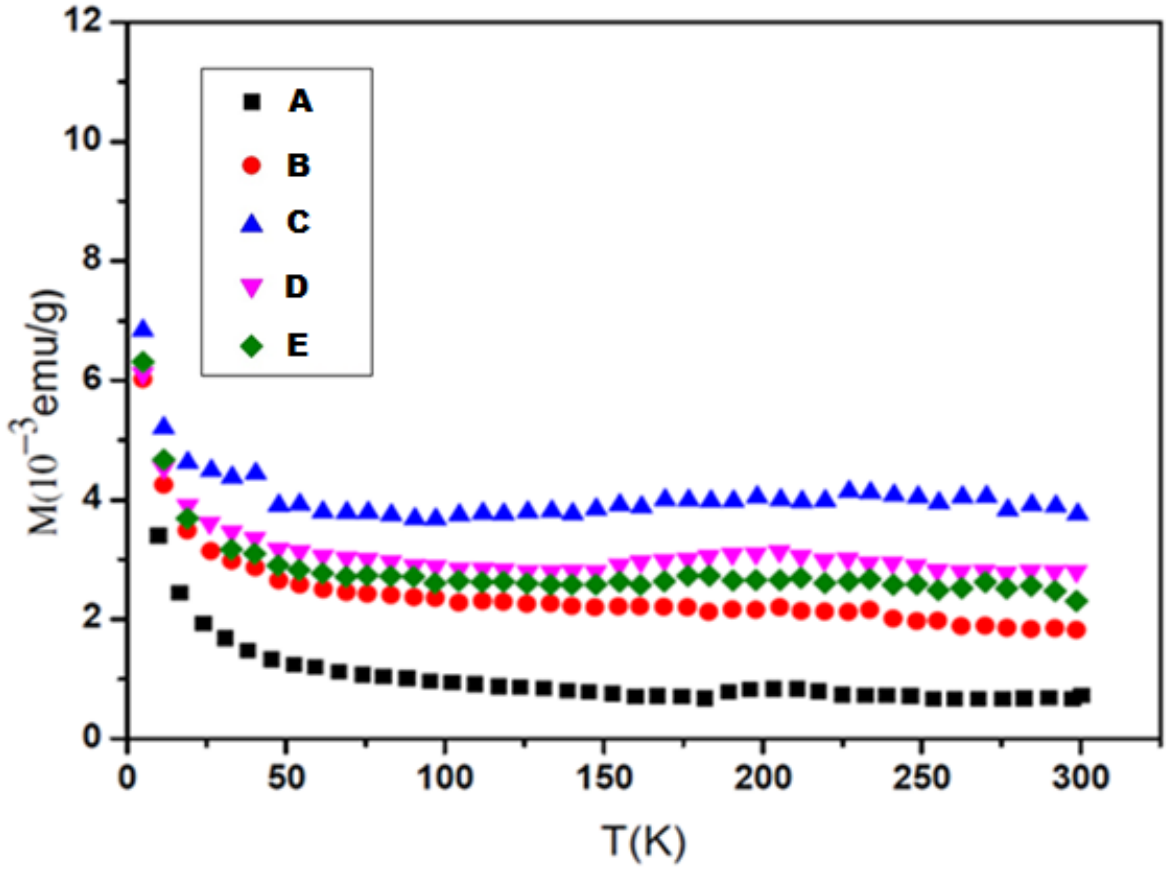

Figure 10

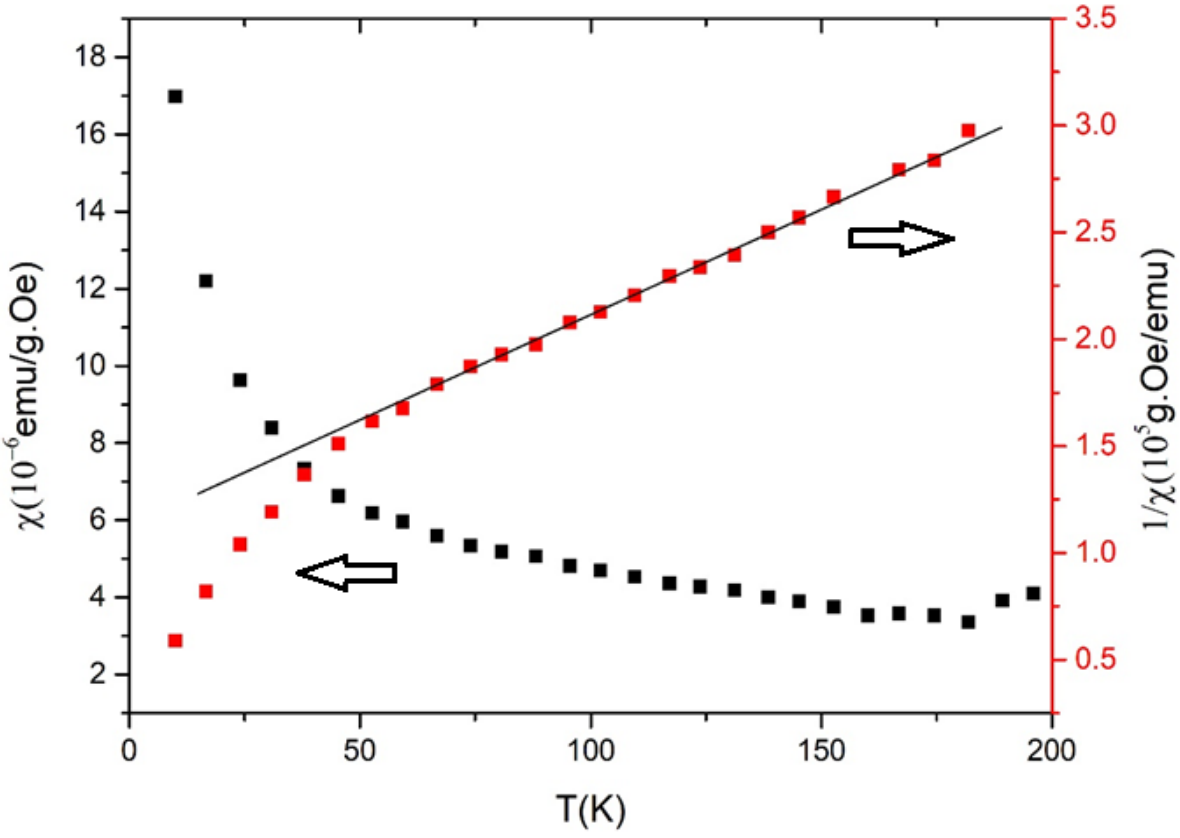
χ(10⁻⁶emu/g.Oe)
1/χ(10⁵g.Oe/emu)
T(K)
0
50
100
150
200
2
4
6
8
10
12
14
16
18
0.5
1.0
1.5
2.0
2.5
3.0
3.5

Figure 11

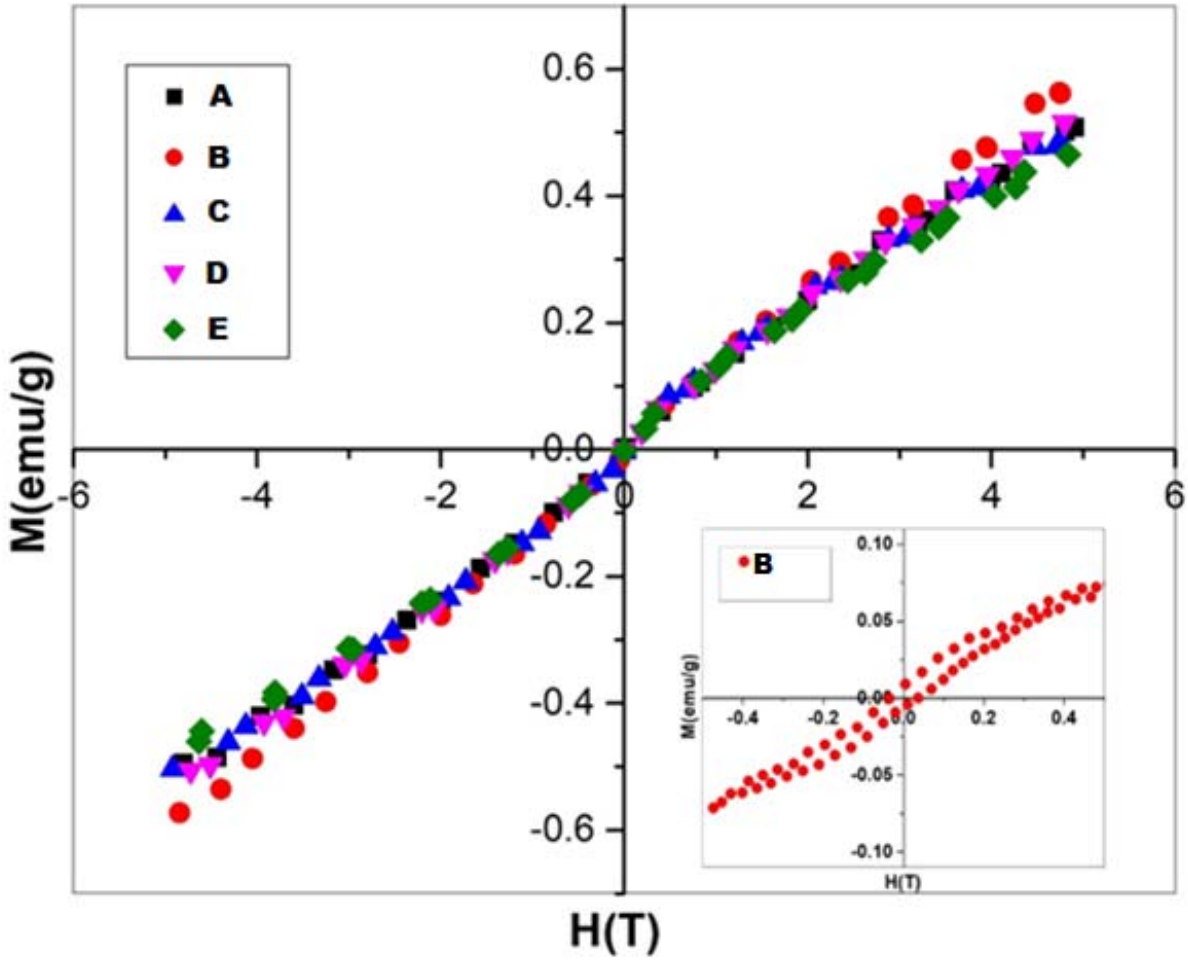
A
B
C
D
E
M(emu/g)
H(T)
0.6
0.4
0.2
0.0
-0.2
-0.4
-0.6
-6
-4
-2
0
2
4
6
B
0.10
0.05
0.00
-0.05
-0.10
-0.4
-0.2
0.0
0.2
0.4
M(emu/g)
H(T)